Ammonium nitrate particles formed in upper troposphere from ground ammonia sources during Asian monsoons

Michael Höpfner [1]*, Jörn Ungermann [2], Stephan Borrmann[3,4], Robert Wagner[1], Reinhold Spang [2], Martin Riese [2,5], Gabriele Stiller [1], Oliver Appel[3,4], Anneke M. Batenburg [3,4], Silvia Bucci [6], Francesco Cairo[7], Antonis Dragoneas[3,4], Felix Friedl-Vallon [1], Andreas Hünig[3,4], Sören Johansson [1], Lukas Krasauskas[2], Bernard Legras [6], Thomas Leisner [1], Christoph Mahnke [3,4], Ottmar Möhler[1], Sergej Molleker[3,4], Rolf Müller [2], Tom Neubert [8], Johannes Orphal[1], Peter Preusse[2], Markus Rex[9], Harald Saathoff[1], Fred Stroh[2], Ralf Weigel[4] and Ingo Wohltmann[9]

The rise of ammonia emissions in Asia is predicted to increase radiative cooling and air pollution by forming ammonium nitrate particles in the lower troposphere. There is, however, a severe lack of knowledge about ammonia and ammoniated aerosol particles in the upper troposphere and their possible effects on the formation of clouds. Here we employ satellite observations and high-altitude aircraft measurements, combined with atmospheric trajectory simulations and cloud-chamber experiments, to demonstrate the presence of ammonium nitrate particles and also track the source of the ammonia that forms into the particles. We found that during the Asian monsoon period, solid ammonium nitrate particles are surprisingly ubiquitous in the upper troposphere from the Eastern Mediterranean to the Western Pacific—even as early as in 1997. We show that this ammonium nitrate aerosol layer is fed by convection that transports large amounts of ammonia from surface sources into the upper troposphere. Impurities of ammonium sulfate allow the crystallization of ammonium nitrate even in the conditions, such as a high relative humidity, that prevail in the upper troposphere. Solid ammonium nitrate particles in the upper troposphere play a hitherto neglected role in ice cloud formation and aerosol indirect radiative forcing.

Particulate ammonium nitrate (NH_4NO_3 (AN)) and ammonium sulfate (($NH_4)_2SO_4$ (AS)) are important species in the tropospheric aerosol system. Ammonia (NH_3), as the most abundant alkaline gas in the atmosphere, is the major precursor for the formation of these aerosols[1,2]. Emissions of NH_3 are estimated to keep rising over the coming decades[3–6]. Model calculations indicate that this will lead to an increase of the reflected solar radiation through AN particles, which are mainly produced in the lower part of the troposphere[7,8]. At upper tropospheric levels, the presence of NH_3 may strongly enhance new particle formation through the stabilization of sulfuric acid clusters, especially at the low temperatures prevalent at altitudes near the tropopause[9,10]. Also in the upper troposphere (UT), solid AS particles were identified as potential ice nucleating particles that affected the formation and radiative properties of cirrus clouds[11]. Yet solid AS, as well as AN particles, remain unobserved on a global scale in the UT. Furthermore, AN is generally assumed to exist as an aqueous solution under UT conditions, so that it cannot promote heterogeneous ice formation[12,13].

The presence of NH_3 in the UT was recently revealed by satellite observations during the Asian monsoon[14]. During that season,

the polluted air masses transported convectively from the boundary layer to high altitudes are confined within the so-called Asian summer monsoon anticyclone (AMA)[15]. In the AMA, pollution accumulates and is dispersed over a large area of the Northern Hemisphere that reaches longitudes from 10 to 140° E and latitudes from 10 to 40° N (refs. [16–21]). In summer, air exported from the AMA influences the composition of the entire lowermost stratosphere of the Northern Hemisphere[22,23].

Connected to the AMA, a layer of enhanced aerosol loading at altitudes of 14–18 km was observed by satellite[24–26] and balloon-borne instruments[27]. Although little is known about the composition of the aerosol particles that form this Asian tropopause aerosol layer (ATAL), its particles are currently believed to consist of carbonaceous and sulfate material, mineral dust[28–31] and nitrate[32]. The ATAL particles are often connected with the presence of pollution markers in the monsoon circulation and large SO_2 emissions in Southeast Asia[26,27]. Observations of the composition of ATAL aerosol particles are, however, sparse. Preliminary data from two single balloon flights indicate the presence of nitrate aerosol particles[27].

[1]Institute of Meteorology and Climate Research, Karlsruhe Institute of Technology, Karlsruhe, Germany. [2]Institute of Energy and Climate Research, Stratosphere, Forschungszentrum Jülich, Jülich, Germany. [3]Particle Chemistry Department, Max Planck Institute for Chemistry, Mainz, Germany. [4]Institute for Atmospheric Physics, Johannes Gutenberg University, Mainz, Germany. [5]Institute for Atmospheric and Environmental Research, University of Wuppertal, Wuppertal, Germany. [6]Laboratoire de Météorologie Dynamique, UMR8539, IPSL, CNRS/PSL-ENS/Sorbonne Université/École polytechnique, Paris, France. [7]Institute of Atmospheric Sciences and Climate, ISAC-CNR, Rome, Italy. [8]Central Institute of Engineering, Electronics and Analytics—Electronic Systems, Forschungszentrum Jülich, Jülich, Germany. [9]Alfred Wegener Institute, Helmholtz Center for Polar and Marine Research, Potsdam, Germany. *e-mail: michael.hoepfner@kit.edu
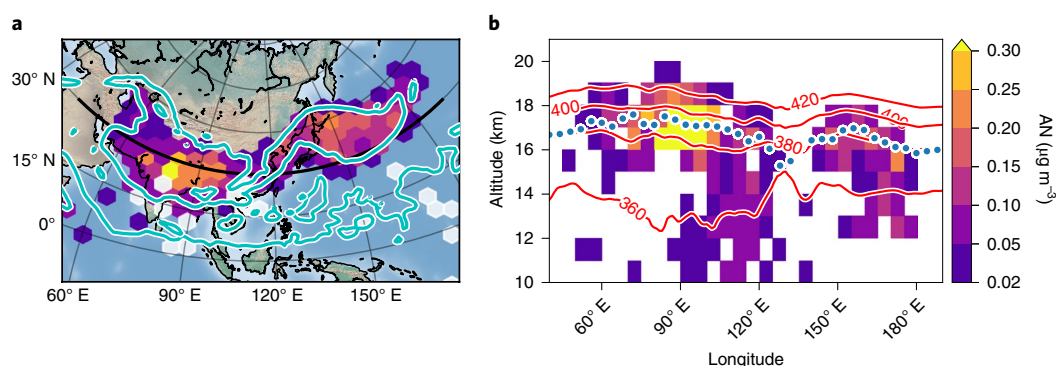
Fig. 1 | AN observed by CRISTA in the UT in 1997. a,b, Cross-sections of synoptically interpolated AN mass concentrations at a potential temperature of 380 K (16–17 km altitude) (**a**) and at 30° N (**b**) derived from CRISTA observations between 8 and 16 August 1997. The cyan line in **a** shows the 4.1 potential vorticity unit contour line, a rough measure for the extent of the AMA core, the white hexagons indicate missing data and the black line the position of the cross-section of **b**. The red lines in **b** show the potential temperature (K) and the blue dots the location of the lapse rate tropopause.

Solid AN discovered by satellite and laboratory measurements

The first evidence of solid AN aerosol particles in the UT was provided by satellite observations with the CRISTA (Cryogenic Infrared Spectrometers and Telescopes for the Atmosphere) instrument inside the AMA in August 1997. We identified a distinct spectral signature at 831 cm^{-1} that is only present in spectra taken inside the AMA as the $\nu_2(NO_3^-)$ band of solid AN (Methods and Supplementary Fig. 1)[33]. Neither aqueous AN nor any other aerosol or trace gas could replicate the observed spectral feature.

We investigated the crystallization behaviour of aqueous AN aerosol particles at the temperature conditions of the UT by AIDA (Aerosol Interaction and Dynamics in the Atmosphere) aerosol and cloud-chamber measurements. In agreement with previous studies that extended down to a temperature of −35 °C (ref. [12]), we did not detect the efflorescence of pure aqueous AN aerosol particles. However, the formation of solid AN was observed for particles composed of aqueous mixtures of AN and AS. At −50 °C, already a fraction of 2.9 mol% AS was sufficient to initiate the crystallization of AN. The crystallization rate was dependent on the ambient relative humidity (RH) with respect to supercooled liquid water. On a timescale of several hours, the formation of solid AN particles was even observed at RHs as high as 61%, which corresponds to an almost ice-saturated environment at −50 °C (Methods and Supplementary Information). By demonstrating that small amounts of sulfate facilitate the formation of solid AN even at a high RH, these experimental results strongly support the satellite detection of solid AN particles within the AMA. Further, the highly resolved laboratory infrared spectra of the $\nu_2(NO_3^-)$ absorption band at low temperatures provide the basis for a quantitative retrieval of the AN particle mass density distributions from satellite and airborne observations (Methods).

The spatially resolved AN observations with the CRISTA satellite reveal that enhanced concentrations of AN (0.05–0.3 µg m^{-3}) are located only within the AMA (Fig. 1). These observations between 8 and 16 August 1997 indicate that an ATAL was present in the Asian monsoon UT in summer 1997, years earlier than hitherto thought[25].

The seasonal and interannual variability of AN concentrations in the AMA between 2002 and 2011 was derived from the analysis of space-borne MIPAS (Michelson Interferometer for Passive Atmospheric Sounding) observations (Methods). Enhanced levels of AN appear in the second half of June, increase in areal coverage and concentration until the mid-to-end of August and reach values comparable to those derived from the CRISTA instrument (Fig. 2a). During these periods, the maximum concentrations are
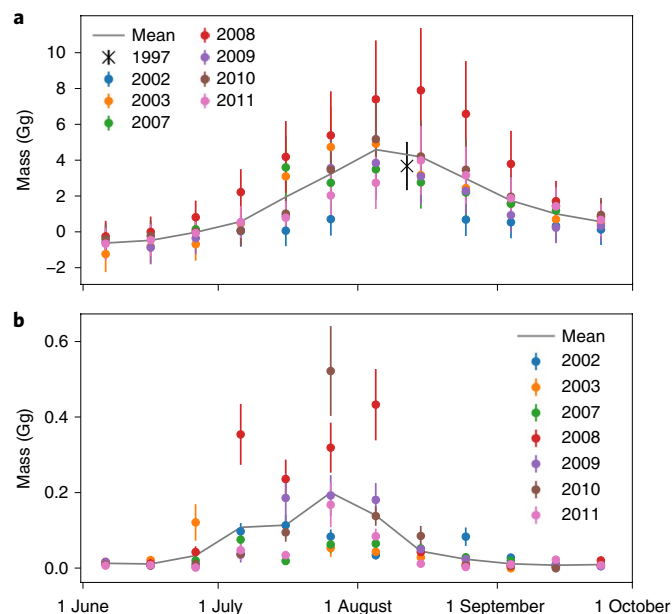

Fig. 2 | Time series of AN and NH$_3$ in the AMA. a,b, Time series of the total mass of AN (**a**) and NH$_3$ (**b**) as derived from MIPAS observations for the region 10–110° E, 20–40° N and 13–17 km altitude. CRISTA observations of AN are included in **a** as a black cross. Error bars are Gaussian combinations of the estimated retrieval errors (Methods) and the s.d. of the mean values.

always located within the confines of the AMA and, for example, reach as far as the Eastern Mediterranean (Supplementary Figs. 5 and 6). This seasonal cycle is modulated by a large interannual variability with a clear maximum in 2008 of values three to four times higher than during the other years.

Simultaneously observed concentrations of NH$_3$ from a new MIPAS data set (Methods) start to increase by the mid-to-end of June, reach a maximum by the mid-to-end of July and vanish towards the end of August (Fig. 2b and Supplementary Figs. 5 and 6). This temporal evolution indicates a delay of 1–2 weeks of the AN maximum with respect to NH$_3$. This is consistent with the notion of advective upward transport in the monsoon anticyclone at potential temperatures above about 360 K, which is much slower than convection[34]. Despite this delay, the onset of the enhanced values of AN and NH$_3$ inside the AMA appears simultaneously by the end of June.
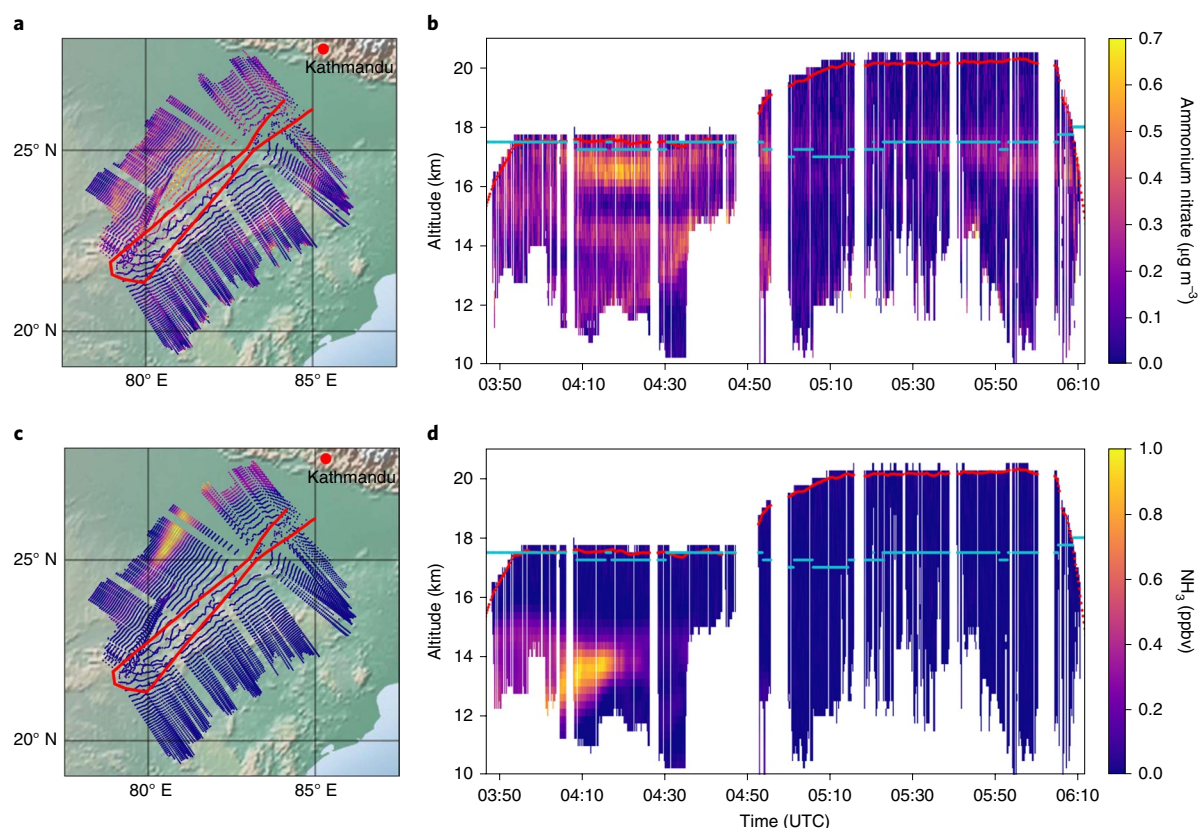
Fig. 3 | Airborne limb-imaging observations of AN and NH₃ in the UT above India during the 2017 Asian monsoon season. a–d, Altitude–time horizontal projections of AN mass densities (**a,b**) and NH₃ VMRs (**c,d**), derived from GLORIA measurements during the Geophysica flight on 31 July 2017. The horizontal projections at the tangent points are given in **a** and **c** and the vertical projections in **b** and **d**. The vertical resolution and estimated uncertainty (precision, accuracy) are: AN, 0.8 km, $\pm 0.03\,\mu g\,m^{-3} \pm 30\%$; NH₃, 0.8 km, $\pm 8\,pptv \pm 20\%$. Red lines, aircraft position (**a** and **c**) and altitude (**b** and **d**); light blue lines, lapse rate tropopause (**b** and **d**). UTC, coordinated universal time.

AN particles observed from aircraft in the UT

High-altitude aircraft flights from Kathmandu, Nepal, in July and August 2017 within the StratoClim project (http://www.stratoclim.org/) provided the first opportunity to measure the distribution and composition of aerosols and trace gases inside the Asian monsoon UT with a variety of in situ and remote sounding instruments. Altitude profiles of AN and NH₃ along the flight track, with a greatly improved resolution compared to that of the satellite products, were obtained from infrared limb-imaging observations with the airborne GLORIA (Gimballed Limb Observer for Radiance Imaging of the Atmosphere) instrument (Methods)[35,36]. Figure 3 presents cross-sections of AN and NH₃ along the flight track on 31 July 2017, which leads from Kathmandu (27.7° N, 85.4° E) southwest to about 21° N, 79° E and back. Owing to the limb-sounding instrument's observational direction to the right of the aircraft, the GLORIA measurements sampled air masses of different origin during the southwest-bound and northeast-bound flight legs. During the southwest-bound flight leg, we observed enhanced concentrations of AN aerosol mass that reached up to $0.7\,\mu g\,m^{-3}$ at around 16–17 km altitude (Fig. 3a,b). The height of this layer coincides with the typical altitude of the ATAL[26] and with our satellite retrievals. During the first part of the flight, a lower region of enhanced AN concentrations of up to $0.5\,\mu g\,m^{-3}$ between 12 km and 15 km altitude was observed.

Distinct layers of enhanced values of the total aerosol volume density are also observed by in situ particle-size distribution measurements during the ascent and descent of the aircraft on 31

July 2017 (Fig. 4a)[37,38] (Methods). These correlate very well with the maxima in the nitrate mass concentration profiles as measured by a flash vaporization and continuous ionization aerosol mass spectrometer (AMS), the ERICA–AMS (ERICA, ERc instrument for the chemical composition of aerosols)[39–41] (Fig. 4b and Methods). Although there is no exact coincidence between remote sensing and in situ measurements, the aerosol layer in the upper part of the profiles above about 15 km is present in both kinds of observation, as well as in a second layer below. The retrieved values of nitrate aerosol mass concentration of around $0.3\,\mu g\,m^{-3}$ from the infrared sounder fit to the independent in situ observations by the mass spectrometer (Supplementary Fig. 7).

Assuming a particle mass density for AN of $1.72\,g\,cm^{-3}$ for the conversion of the observed aerosol volume densities to NO₃⁻ mass concentrations, the resulting maximum values at 13–14 and 16 km agree with the mass spectrometric data within the error margins. Thus, the hypothesis that a major fraction of the ATAL particle mass consists of AN is consistent with the observed aerosol volume densities at peak NO₃⁻ mass concentrations.

Additionally, the ERICA laser ablation aerosolmass spectrometer (LAMS) detected the simultaneous presence of sulfate and nitrate in the mass spectra of individual single particles (Methods and Supplementary Fig. 9). Such a common occurrence of both components was observed in more than 91% of the particles analysed between 10 and 17 km during the flight on 31 July 2017. These findings corroborate the results from the cloud-chamber observations on the crystallization behaviour of aqueous AS/AN mixtures.
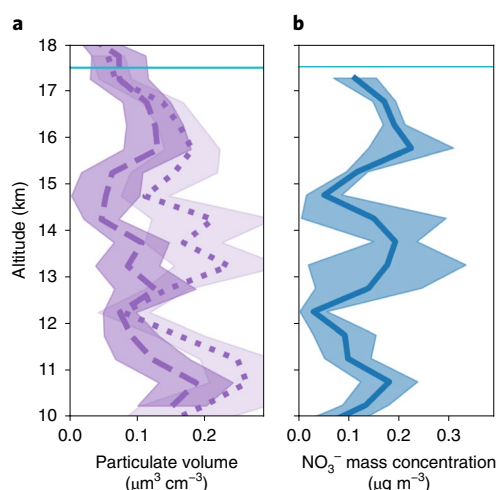
Fig. 4 | Airborne in situ aerosol observations in the Asian monsoon UT on 31 July 2017. a, Ultra-high sensitivity aerosol spectrometer (UHSAS)- and condensation particle counting system (COPAS)-derived aerosol volume density during the ascent (dashed) and the descent (dotted) at Kathmandu. **b**, ERICA–AMS particulate NO_3^- mass concentrations. The values are averages in vertical bins of 0.25 km. For the nitrate content of ERICA–AMS, the uncertainty is estimated to be 30%. The estimated uncertainty of the UHSAS and COPAS data are below 30%. Light blue horizontal lines, the lapse rate tropopause.

Ground NH_3 as the source of upper tropospheric AN particles

The region of enhanced AN at a 12–15 km altitude during the first part of the flight (Fig. 3a,b) frames a zone of maximum concentrations of NH_3 (Fig. 3c,d). In this region, NH_3 volume mixing ratios (VMRs) reach values of 1 ppbv (parts per billion by volume) at 13.5 km altitude. During the previous flight, on 29 July 2017, NH_3 mixing ratios of even 1.4 ppbv were encountered at similar altitudes. These concentrations are up to 40 times higher than the values reported previously[14], and are, thus, by far the highest concentrations of NH_3 ever observed in the UT.

The high AN mass concentrations observed close to the region of enhanced mixing ratios of NH_3 might either be due to similar source regions or to newly formed AN particles through a gas-to-particle conversion within the plume of the elevated NH_3 concentrations. Conversion of the NH_3 VMRs to equivalent AN mass concentrations leads to maximum values of up to 1 μg m^{-3}. Thus, the GLORIA measurements of that particular day show sufficiently high values of the gas-phase NH_3 mixing ratios to explain concentrations up to 0.7 μg m^{-3} of AN.

We studied the possible origin of the elevated NH_3 concentrations in the UT by trajectory analyses in combination with satellite data of total column amounts of NH_3 (ref. [42]) (Methods and Supplementary Figs. 10 and 11). During the days prior to our aircraft measurements, enhanced column amounts of NH_3 were observed at lower atmospheric levels in the region of northwest India and northeast Pakistan, a region known as a hot spot for NH_3 emissions[6,43,44]. Trajectory simulations suggest that the high amounts of NH_3 observed by the GLORIA instrument were initially transported convectively to altitudes of 12–14 km. Subsequently, they were advected by the anticyclonic upper tropospheric monsoon circulation to the location of the airborne observations within a few days. These measurements prove that NH_3 reaches the UT in amounts sufficient to explain the mass density of AN observed. The relevant processes that reduce the impact of the washout of NH_3 during convection might involve a low acidity of convective rain droplets[45] or a release of NH_3 during the freezing process of cloud particles[46–48].

We uncovered that a considerable part of the aerosol particles in the AMA consists of solid AN being formed through the convective uplift of NH_3 from intense surface emissions. Owing to its longer lifetime, AN is subsequently transported vertically and horizontally inside the AMA, and thereby already influences a large area of the Northern Hemisphere. Air masses with an enhanced concentration of AN are not confined within the AMA, but are transported either into the lowermost stratosphere at mid-latitudes or into the tropical belt. Here, owing to dilution, the AN concentrations are no longer visible in our satellite data. It is highly probable that, in the UT, these solid particles act as effective ice-nucleating particles, as previously demonstrated for solid AS[11].

In the future, rising emissions of NH_3 will probably also lead to a change of AN particles in the UT with potential consequences for the Earth's radiative budget. For quantitative assessments using chemical–dynamical models, a better quantification of the NH_3 surface emissions over the Indian subcontinent as well as a deeper understanding of the interaction processes of NH_3 with liquid water and ice during convection is needed. Furthermore, it is most important to characterize the ice-nucleating capacity of solid AN particles.

Online content

Any methods, additional references, Nature Research reporting summaries, source data, statements of code and data availability and associated accession codes are available at https://doi.org/10.1038/s41561-019-0385-8 .

References

1. Dentener, F. J. & Crutzen, P. J. A three-dimensional model of the global ammonia cycle. *J. Atmos. Chem.* **19**, 331–369 (1994).
2. Behera, S. N., Sharma, M., Aneja, V. P. & Balasubramanian, R. Ammonia in the atmosphere: a review on emission sources, atmospheric chemistry and deposition on terrestrial bodies. *Environ. Sci. Pollut. Res.* **20**, 8092–8131 (2013).
3. Bouwman, A. et al. A global high-resolution emission inventory for ammonia. *Glob. Biogeochem. Cycles* **11**, 561–587 (1997).
4. Erisman, J. W., Sutton, M. A., Galloway, J., Klimont, Z. & Winiwarter, W. How a century of ammonia synthesis changed the world. *Nat. Geosci.* **1**, 636–639 (2008).
5. Warner, J. X. et al. Increased atmospheric ammonia over the world's major agricultural areas detected from space. *Geophys. Res. Lett.* **44**, 2875–2884 (2017).
6. Xu, R. T. et al. Half-century ammonia emissions from agricultural systems in southern Asia: magnitude, spatiotemporal patterns, and implications for human health. *Geohealth* **2**, 40–53 (2018).
7. Hauglustaine, D. A., Balkanski, Y. & Schulz, M. A global model simulation of present and future nitrate aerosols and their direct radiative forcing of climate. *Atmos. Chem. Phys.* **14**, 11031–11063 (2014).
8. IPCC *Climate Change 2013: The Physical Science Basis* (eds Stocker, T. F. et al.) (Cambridge Univ. Press, 2013).
9. Kirkby, J. et al. Role of sulphuric acid, ammonia and galactic cosmic rays in atmospheric aerosol nucleation. *Nature* **476**, 429–433 (2011).
10. Kürten, A. et al. Experimental particle formation rates spanning tropospheric sulfuric acid and ammonia abundances, ion production rates, and temperatures. *J. Geophys. Res.* **121**, 12377–12400 (2016).
11. Abbatt, J. P. D. et al. Solid ammonium sulfate aerosols as ice nuclei: a pathway for cirrus cloud formation. *Science* **313**, 1770–1773 (2006).
12. Cziczo, D. J. & Abbatt, J. P. D. Infrared observations of the response of NaCl, MgCl$_2$, NH$_4$HSO$_4$, and NH$_4$NO$_3$ aerosols to changes in relative humidity from 298 to 238 K. *J. Phys. Chem. A* **104**, 2038–2047 (2000).
13. Cziczo, D. J. & Abbatt, J. P. D. Ice nucleation in NH$_4$HSO$_4$, NH$_4$NO$_3$, and H$_2$SO$_4$ aqueous particles: implications for cirrus cloud formation. *Geophys. Res. Lett.* **28**, 963–966 (2001).
14. Höpfner, M. et al. First detection of ammonia (NH$_3$) in the Asian summer monsoon upper troposphere. *Atmos. Chem. Phys.* **16**, 14357–14369 (2016).
15. Ploeger, F. et al. A potential vorticity-based determination of the transport barrier in the Asian summer monsoon anticyclone. *Atmos. Chem. Phys.* **15**, 13145–13159 (2015).
16. Park, M., Randel, W. J., Gettelman, A., Massie, S. T. & Jiang, J. H. Transport above the Asian summer monsoon anticyclone inferred from Aura Microwave Limb Sounder tracers. *J. Geophys. Res.* **112**, D16309 (2007).

17. Park, M. et al. Chemical isolation in the Asian monsoon anticyclone observed in Atmospheric Chemistry Experiment (ACE-FTS) data. *Atmos. Chem. Phys.* **8**, 757–764 (2008).

18. Randel, W. J. et al. Asian monsoon transport of pollution to the stratosphere. *Science* **328**, 611–613 (2010).

19. Ungermann, J. et al. Observations of PAN and its confinement in the Asian summer monsoon anticyclone in high spatial resolution. *Atmos. Chem. Phys.* **16**, 8389–8403 (2016).

20. Santee, M. L. et al. A comprehensive overview of the climatological composition of the Asian summer monsoon anticyclone based on 10 years of Aura microwave limb sounder measurements. *J. Geophys. Res.* **122**, 5491–5514 (2017).

21. Lelieveld, J. et al. The South Asian monsoon: pollution pump and purifier. *Science* **361**, 270–273 (2018).

22. Ploeger, F., Konopka, P., Walker, K. & Riese, M. Quantifying pollution transport from the Asian monsoon anticyclone into the lower stratosphere. *Atmos. Chem. Phys.* **17**, 7055–7066 (2017).

23. Yu, P. et al. Efficient transport of tropospheric aerosol into the stratosphere via the Asian summer monsoon anticyclone. *Proc. Natl Acad. Sci. USA* **114**, 6972–6977 (2017).

24. Vernier, J.-P., Tomason, L. W. & Kar, J. CALIPSO detection of an Asian tropause aerosol layer. *Geophys. Res. Lett.* **38**, L07804 (2011).

25. Thomason, L. W. & Vernier, J.-P. Improved SAGE II cloud/aerosol categorization and observations of the Asian tropopause aerosol layer: 1989–2005. *Atmos. Chem. Phys.* **13**, 4605–4616 (2013).

26. Vernier, J. P. et al. Increase in upper tropospheric and lower stratospheric aerosol levels and its potential connection with Asian pollution. *J. Geophys. Res.* **120**, 1608–1619 (2015).

27. Vernier, J.-P. et al. BATAL: the balloon measurement campaigns of the Asian tropopause aerosol layer. *Bull. Am. Meteorol. Soc.* **99**, 955–973 (2018).

28. Fadnavis, S. et al. Transport of aerosols into the UTLS and their impact on the Asian monsoon region as seen in a global model simulation. *Atmos. Chem. Phys.* **13**, 8771–8786 (2013).

29. Neely, R. R. et al. The contribution of anthropogenic SO₂ emissions to the Asian tropopause aerosol layer. *J. Geophys. Res.* **119**, 1571–1579 (2014).

30. Yu, P., Toon, O. B., Neely, R. R., Martinsson, B. G. & Brenninkmeijer, C. A. M. Composition and physical properties of the Asian tropopause aerosol layer and the North American tropospheric aerosol layer. *Geophys. Res. Lett.* **42**, 2540–2546 (2015).

31. Lau, W. K. M., Yuan, C. & Li, Z. Origin, maintenance and variability of the Asian Tropopause Aerosol Layer (ATAL): the roles of monsoon dynamics. *Sci. Rep.* **8**, 3960 (2018).

32. Gu, Y., Liao, H. & Bian, J. Summertime nitrate aerosol in the upper troposphere and lower stratosphere over the Tibetan Plateau and the South Asian summer monsoon region. *Atmos. Chem. Phys.* **16**, 6641–6663 (2016).

33. Schlenker, J. C. & Martin, S. T. Crystallization pathways of sulfate–nitrate–ammonium aerosol particles. *J. Phys. Chem. A* **109**, 9980–9985 (2005).

34. Vogel, B. et al. Lagrangian simulations of the transport of young air masses to the top of the Asian monsoon anticyclone and into the tropical pipe. *Atmos. Chem. Phys.* **19**, 6007–6034 (2019).

35. Friedl-Vallon, F. et al. Instrument concept of the imaging Fourier transform spectrometer GLORIA. *Atmos. Meas. Tech.* **7**, 3565–3577 (2014).

36. Riese, M. et al. Gimballed limb observer for radiance imaging of the atmosphere (GLORIA) scientific objectives. *Atmos. Meas. Tech.* **7**, 1915–1928 (2014).

37. Cai, Y., Montague, D. C., Mooiweer-Bryan, W. & Deshler, T. Performance characteristics of the ultra high sensitivity aerosol spectrometer for particles between 55 and 800 nm: laboratory and field studies. *J. Aerosol Sci.* **39**, 759–769 (2008).

38. Weigel, R. et al. In situ observations of new particle formation in the tropical upper troposphere: the role of clouds and the nucleation mechanism. *Atmos. Chem. Phys.* **11**, 9983–10010 (2011).

39. Drewnick, F. et al. A new time-of-flight aerosol mass spectrometer (TOF-AMS)—instrument description and first field deployment. *Aerosol Sci. Technol.* **39**, 637–658 (2005).

40. Allan, J. D. et al. A generalised method for the extraction of chemically resolved mass spectra from aerodyne aerosol mass spectrometer data. *J. Aerosol Sci.* **35**, 909–922 (2004).

41. Schulz, C. et al. Aircraft-based observations of isoprene-epoxydiol-derived secondary organic aerosol (IEPOX-SOA) in the tropical upper troposphere over the Amazon region. *Atmos. Chem. Phys.* **18**, 14979–15001 (2018).

42. Van Damme, M. et al. Version 2 of the IASI NH₃ neural network retrieval algorithm: near-real-time and reanalysed datasets. *Atmos. Meas. Tech.* **10**, 4905–4914 (2017).

43. Clarisse, L., Clerbaux, C., Dentener, F., Hurtmans, D. & Coheur, P.-F. Global ammonia distribution derived from infrared satellite observations. *Nat. Geosci.* **2**, 479–483 (2009).

44. van Damme, M. et al. Industrial and agricultural ammonia point sources exposed. *Nature* **564**, 99–103 (2018).

45. Metzger, S., Dentener, F., Krol, M., Jeuken, A. & Lelieveld, J. Gas/aerosol partitioning 2. Global modeling results. *J. Geophys. Res.* **107**, 4313 (2002).

46. Hoog, I., Mitra, S. K., Diehl, K. & Borrmann, S. Laboratory studies about the interaction of ammonia with ice crystals at temperatures between 0 and −20 °C. *J. Atmos. Chem.* **57**, 73–84 (2007).

47. Jost, A., Szakáll, M., Diehl, K., Mitra, S. K. & Borrmann, S. Chemistry of riming: the retention of organic and inorganic atmospheric trace constituents. *Atmos. Chem. Phys.* **17**, 9717–9732 (2017).

48. Ge, C., Zhu, C., Francisco, J. S., Zeng, X. C. & Wang, J. A molecular perspective for global modeling of upper atmospheric NH₃ from freezing clouds. *Proc. Natl Acad. Sci. USA* **115**, 6147–6152 (2018).

Author contributions

M.H. conducted the analysis of MIPAS and GLORIA data, produced Figs. 2–4 and wrote the paper with all the authors contributing. J.U. conducted the analysis of the CRISTA data, helped with analysis of the GLORIA data and produced Fig. 1. A.D., S.M., A.M.B., O.A., A.H. and S. Borrmann performed and analysed the aircraft in situ measurements of ERICA. C.M. and R. Weigel prepared the analyses for Fig. 4a and O.A. for Fig. 4b. C.M. and R. Weigel conducted the measurements and data analyses for UHSAS and COPAS, respectively. R. Wagner, H.S., O.M. and T.L. conceived and performed the AIDA experiments and contributed to their interpretation. R.S. discovered the AN emission feature in the CRISTA data. M. Riese conceived the reanalysis of the CRISTA data with respect to signals of the ATAL. G.S. contributed to the analysis of the MIPAS data. B.L. and S. Bucci conducted the TRACZILLA trajectory calculations. F.C. performed the MAS aircraft observations and conducted their analysis. F.F.-V. conducted the GLORIA aircraft observations. S.J. analysed the trajectory data sets in combination with the IASI measurements. S.J. and L.K. helped with the analysis of the GLORIA data. P.P. contributed to the CRISTA and GLORIA data analysis. T.N. helped to perform the GLORIA observations. R.M. contributed to the interpretation of the observations. J.O. contributed to the interpretation of spectroscopic issues with AN and NH₃. F.S. and M. Rex. defined the flight region, the general approach, general flight patterns and instrumentation of the aircraft campaign and organized it. I.W. developed the ATLAS model and provided the trajectory calculations from it, with contributions from M. Rex.

Competing interests

The authors declare no competing interests.

Additional information

Supplementary information is available for this paper at https://doi.org/10.1038/s41561-019-0385-8 .

Reprints and permissions information is available at www.nature.com/reprints.

Correspondence and requests for materials should be addressed to M.H.

Publisher's note: Springer Nature remains neutral with regard to jurisdictional claims in published maps and institutional affiliations.

Methods

Cloud-chamber observations. The AIDA aerosol and cloud chamber is a highly instrumented 84.5 m³ aluminium vessel that can be operated at temperatures between +60 and −90 °C (ref. [49]). The ambient RH can be controlled by evaporating a specified amount of water vapour into the chamber. The number concentration and size distribution of the aerosol particles added to the chamber were measured with a condensation particle counter (model 3010 (TSI)), a scanning mobility particle sizer (model 3071A (TSI)) and an aerodynamic particle spectrometer (model 3321 (TSI)). RH was measured in situ by tunable diode laser absorption spectroscopy, by using a rotational–vibrational water vapour absorption line at 1.37 µm (ref. [50]). Infrared extinction spectra of the aerosol particles were recorded in situ with a Fourier transform infrared spectrometer (model IFS66v (Bruker)) coupled to a multiple reflection cell (optical path length 166.8 m, wavenumber range 6,000–800 cm⁻¹ and 0.5 cm⁻¹ resolution)[51]. With polarization-resolved in situ laser light scattering measurements, the backscattering linear depolarization ratio of the aerosol particles at a scattering angle of 178° and a wavelength of 488 nm were determined[52]. Owing to the different infrared spectral signatures of liquid and solid AN, as well as the different depolarization levels of spherical aqueous AN solution droplets and aspherical crystalline AN particles, both the infrared and depolarization measurements allow us to study the phase change behaviour of the added aerosol particles. A schematic of the AIDA facility and further details about its optical instrumentation are given in Wagner et al.[53].

For our experiments, the AIDA chamber was held at −50 °C and two different RHs with respect to supercooled water, that is, at 22 and 61% RH, to simulate dry and humid upper tropospheric air masses. The aerosol particles were generated from aqueous solutions of 100 mol% AN, 90 mol% AN + 10 mol% AS and 97.1 mol% AN + 2.9 mol% AS. The bulk solutions were prepared by dissolving the respective chemicals (AN 99% (VWR Chemicals) and AS 99.5% (Merck)) in high-purity water (GenPure Pro UV ultrapure water system (Thermo Scientific)) with an overall solute concentration of 10 wt%. Aqueous solution droplets were produced with an ultrasonic nebulizer (GA 2400 (SinapTec)). The aerosol flow first passed a set of silica gel diffusion dryers (Topas GmbH) to reduce the RH in the aerosol flow to ≤3% and was then injected into the AIDA chamber through a stainless-steel tube. The spectrum of liquid AN shown in Supplementary Fig. 1 was recorded after the injection of the 100 mol% AN solution into the AIDA chamber at 61% RH, whereas the spectrum of the crystalline phase was recorded for the 97.1 mol% AN + 2.9 mol% AS mixture at 22% RH. The pertinent details of these experiments are further discussed in the Supplementary Information.

To derive the mass-specific absorption coefficients of the recorded $\nu_2(NO_3^-)$ infrared absorption band of crystalline AN (Supplementary Fig. 1), which were to be used as input for the aerosol mass density retrievals from the satellite observations, we computed the total mass concentration of the aerosol particles suspended in the AIDA chamber. In the first step, the volume size distribution of the aerosol particles was computed from the combination of the scanning mobility particle sizer and aerodynamic particle spectrometer size spectra, employing a particle density of 1.72 g cm⁻³ and a dynamic shape factor of 1.1 to convert the mobility and aerodynamic diameters from the scanning mobility particle sizer and aerodynamic particle spectrometer measurements into an equal-volume sphere diameter (Supplementary Fig. 3). The integrated volume concentration was then multiplied with the particle density to yield the total mass concentration of the crystallized particle ensemble. Finally, the smaller mass fraction of AS, which does not contribute to the signature of the $\nu_2(NO_3^-)$ absorption band at 831 cm⁻¹, was subtracted to yield the mass concentration of AN only. The uncertainty for the AN mass density, which mainly arises from the uncertainties associated with the employed values for the particle density and the dynamic shape factor, was estimated as ±30%.

Remote sensors. *CRISTA.* The Space Shuttle experiment CRISTA was flown on the Shuttle Pallet Satellite in November 1994 (STS 66) and August 1997 (STS 85)[54–56]. The instrument was equipped with three optical telescopes and four spectrometers that covered spectral ranges from 140 to 2,500 cm⁻¹ using 26 detectors. The spectral resolution was $\lambda/\Delta\lambda \approx 500$, with wavelength λ. In the spectral range around 800 cm⁻¹, this corresponds to a resolution of ~1.5 cm⁻¹. During CRISTA-2 (STS85), the main measurement mode covered tangent heights from 11 to 75 km with a vertical sampling step of 2 km and a vertical field-of-view width of about 1.5 km. The horizontal sampling pattern of this mode was 200 km along track and 650 km across track.

MIPAS. The limb sounder MIPAS (Michelson interferometer for passive atmospheric sounding) was in operation between 2002 and 2012 on board the polar orbiting satellite Envisat[57]. It recorded atmospheric emission spectra in the thermal infrared region between 685 and 2,410 cm⁻¹ with spectral resolutions of 0.025 cm⁻¹ in the first measurement period from July 2002 to March 2004 and 0.0625 cm⁻¹ during the second period from January 2005 to April 2012. In the nominal rearward viewing limb-scan mode, tangent altitudes covered regions between 7 and 72 km with a vertical sampling of 3 km up to 42 km in the period 2002–2004 and 1.5 km up to 22 km during 2005–2012. The along-track sampling distance between limb scans was 550 km during the first and 420 km during the

second measurement period. Retrievals were performed on the basis of level-1B calibrated radiances version 5.02/5.06 provided by the European Space Agency.

GLORIA. The airborne limb-imaging spectrometer GLORIA covers the mid-infrared spectral range from 780 to 1,400 cm⁻¹ (refs. [35,36]). During the StratoClim monsoon campaign, GLORIA was deployed on the Geophysica high-altitude aircraft to perform limb observations with an azimuth of 90° to the right-hand side. Geophysica is a Russian high-altitude aircraft of the type M55, built and operated by the Myasishchev Design Bureau. GLORIA takes one limb image of 128 vertical × 48 horizontal pixels with a spectral resolution of 0.0625 cm⁻¹ within 13 s. The vertical elevation coverage is 4.1°. The spectra of the horizontal pixel rows are averaged for noise reduction. In combination with the typical velocity of the aircraft of 700–750 km h⁻¹, this corresponds to an along-track sampling of around 3 km. The generation of calibrated spectra from the GLORIA observations is described in Kleinert et al.[58].

Identification and retrieval of AN from infrared limb observations. In previous infrared limb observations, the infrared ν_2 out-of-plane deformation band of NO_3^- in nitric acid trihydrate (NAT) at 821 cm⁻¹ (refs. [59–61]) was used to detect and quantify NAT particles within polar stratospheric clouds[62–64]. This spectral band is especially suited for detection from limb-viewing sensors as it is located in one of the window regions in the mid-infrared least affected by trace gas signatures. Further, compared to other spectral bands of solids, the nitrate ν_2 band is so sharp that it can easily be identified.

The $\nu_2(NO_3^-)$ band of AN has frequently been assigned in laboratory spectra to wavenumbers around 831 cm⁻¹: 830 cm⁻¹ (ref. [65]), 831–833 cm⁻¹ (ref. [66]), 830–832 cm⁻¹ (ref. [60]) and 831 cm⁻¹ (ref. [33]). The only field observations in which the $\nu_2(NO_3^-)$ band was identified in collected samples of ambient aerosols are reported in Allen et al.[67] and, tentatively, in Hopey et al.[68].

Supplementary Figs. 1 and 4 show the detection of the $\nu_2(NO_3^-)$ band of AN in infrared spectra of the space-borne limb sounding instruments CRISTA and MIPAS, also observed by GLORIA during the StratoClim aircraft campaign. From difference spectra of the observations at similar tangent altitudes but at different locations, a spectral band with a maximum close to 831 cm⁻¹ and a width of about 3 cm⁻¹ could clearly be identified—exactly at the position of the $\nu_2(NO_3^-)$ band of AN. An intensive search for an alternative explanation of this signature, either by other kinds of aerosol particles or by gas-phase species, was not successful. For example, AS, ammonium bisulfate ($(NH_4)HSO_4$) and letovicite ($(NH_4)_3H(SO_4)_2$) do not show any band around 830 cm⁻¹ (refs. [69,70]) and neither do mineral dust[71] and dicarboxylic acids like oxalic acid ($C_2H_2O_4$), malonic acid ($C_3H_4O_4$) (ref. [72]) and succinic acid ($C_4H_6O_4$) (ref. [73]). Apart from NAT and AN, other nitrates, do show the sharp peak of the $\nu_2(NO_3^-)$ band in the 820–840 cm⁻¹ region of the infrared spectrum, but not at the position of AN, for example, sodium nitrate ($NaNO_3$) at 836 cm⁻¹ (refs. [74,75]) or potassium nitrate (KNO_3) at 825 cm⁻¹ (ref. [74]).

As shown in our AIDA measurements as well as in Schlenker and Martin[33], an aqueous solution of AN also has a spectral signature in that spectral region (Supplementary Fig. 3). However, it is clearly distinct from the solid AN peak as its maximum is located at 829 cm⁻¹ and its width is about twice the width of the solid AN signature. Thus, it does not fit our observed spectra (Supplementary Figs. 1 and 4). We therefore conclude that the spectral signature consistently observed inside the AMA by the three different instruments is caused by an aerosol composed of AN in the solid state.

The absorption coefficients, as derived from the aerosol chamber experiments, were used for the retrieval of vertical profiles of the AN mass density from observations from CRISTA, MIPAS and GLORIA. For MIPAS and GLORIA, the same processing scheme as used for NH₃ (see below) was applied. For the analysis of CRISTA observations, the retrieval employed the processing scheme of the airborne successor instrument already used to derive peroxyacetyl nitrate in the AMA[19,76]; the measurement density was improved by synoptically interpolating the measurements of five measurement days to a single point of time in the middle by using trajectory calculations. The spectral window between 828 and 835 cm⁻¹ has been commonly evaluated. Uncertainties for the AN mass concentrations are estimated to be ±0.03 µg m⁻³ (single profile precision) ±10% (systematic instrumental/retrieval) ±30% (spectroscopic AN absorption coefficients from the AIDA observations) for GLORIA, ±15% (single profile precision) ±15% (systematic instrumental/retrieval) ±30% (spectroscopy AN) for CRISTA and ±0.015 µg m⁻³ (single profile precision) ±30% ± 0.01 µg m⁻³ (systematic instrumental/retrieval) ±30% (spectroscopy AN) in the case of MIPAS. The values of the vertical resolutions are 0.8 km for GLORIA, 2.2 km for CRISTA and 4.5 km and 3.5 km for the retrieval from the MIPAS observational periods 1 and 2, respectively.

Identification and retrieval of NH₃ from infrared limb observations. Passive remote sounding is especially suited for the detection of NH₃ as it avoids problems connected to wall effects[77,78]. Retrievals of the NH₃ vertical VMR profiles from MIPAS mean radiance spectra averaged over three months and 10° latitude × 10° longitude are published in Höpfner et al.[14]. To obtain a better resolution in time and space, here we performed retrievals of NH₃ from single MIPAS limb scans. The profile retrievals were performed as in Höpfner et al.[14]. The inversion scheme

is a non-linear least-squares fitting in a global-fit approach on 1 km spaced altitude levels[79] regularized by a first-order smoothing operator[80]. The selected spectral windows with NH_3 signatures are 965.1–965.6 cm^{-1} and 966.6–967.5 cm^{-1} for the first MIPAS period and 965.125–965.625 cm^{-1} and 966.625–967.5 cm^{-1} for the second period. The resulting profiles of the NH_3 VMR are characterized by a vertical resolution of 4–4.5 km and 3.5–4 km (first and second period, respectively). Uncertainties are estimated according to Höpfner et al.[14] to ±5 pptv (single profile precision) and ±15% (accuracy).

As in the case of MIPAS, inversion of the vertical profiles of NH_3 VMRs from GLORIA calibrated limb radiances was performed by the application of a constrained non-linear least-squares fitting scheme, whereby measurements from all the infrared spectra of one GLORIA image are used[81,82]. The retrievals employ an altitude grid spacing of 0.25 km. For the spectral fit, the same spectral windows and inversion procedure as in the case of the MIPAS second measurement period were used (see above). Supplementary Fig. 8 shows the spectral evidence for NH_3 from GLORIA observations taken at a tangent altitude of 13.7 km during the flight on 31 July 2017 at 4:14 coordinated universal time where the retrieval resulted in a value of 920 pptv at the 13.75 km altitude level. Here the spectral emission lines of NH_3 were clearly identified by comparing the simulations with NH_3 to the simulations without NH_3. This proves unambiguously the presence of NH_3 with concentrations near 1 ppbv in the UT. The vertical resolution of the retrieved profiles is about 0.8 km. The VMR profile uncertainties are estimated based on various parameter uncertainties as described in Woiwode et al.[81] and Johansson et al.[82]. They amount to ±8 pptv (single profile precision) and ±20% (accuracy).

In situ sensors on board the Geophysica. *ERICA.* The mass spectrometer ERICA is a newly developed in situ instrument that combines a laser ablation aerosol mass spectrometer (LAMS) similar to Brands et al.[83] and Murphy and Thomson[84] with a flash vaporization–electron impact ionization mass spectrometer (ERICA–AMS) based on the Aerodyne AMS principle[39]. For a quantitative comparison of the aerosol chemical composition, mostly data from the AMS component of ERICA were considered in this study. Here small ensembles of the sampled aerosol particles with size diameters between 60 nm and approximately 2 μm were vaporized at 600 °C followed by electron impact ionization of the vapour[39]. The positive ions were detected by a time-of-flight mass spectrometer from which the particle chemical composition was inferred[40]. Although the reproducibility in the laboratory was better than 5% from calibration to calibration, the uncertainty for the aircraft deployment was estimated to be ±30%. The single-particle aerosol composition was determined by the LAMS component of ERICA, which covered a size range from 150 nm to 2 μm. For each ablated and analysed aerosol particle, the positive and negative ion mass spectra were concurrently recorded by two time-of-flight mass spectrometers. In this way it was possible to unambiguously identify individual particles that contained both sulfate and nitrate, as can be seen from the example mass spectra in Supplementary Fig. 9. The ERICA–LAMS and ERICA–AMS instrument combinations itself and the corresponding sampling inlet system were custom designed similar to those in Schulz et al.[41] for operation on the high-altitude research aircraft Geophysica.

UHSAS/COPAS. The ambient aerosol volume density was obtained from particle-size distribution measurements by means of an in-house modified UHSAS optical particle counter[37] (mounted underneath the aircraft's wing) and the high-altitude COPAS condensation particle counter[38]. The UHSAS covers particle size diameters that range from 65 nm to 1 μm and was modified to operate under stratospheric conditions. One more size bin that extended from 10 to 65 nm was derived as a composite from the COPAS and UHSAS data.

Multiwavelength aerosol scatterometer. The multiwavelength aerosol scatterometer obtained in situ measurements of the aerosol backscatter ratio at 532 nm (ref. [85]).

Trajectory calculations. Two different models for the estimation of convective events along backward trajectories starting at the GLORIA measurement locations were used, TRACZILLA and ATLAS.

The TRACZILLA diffusive back trajectories[86] were calculated based on European Reanalysis 5 (ERA5) reanalysis data (0.25° × 0.25° horizontal resolution, 137 vertical levels and hourly temporal resolution) using kinematic vertical winds. Clusters of 1,000 parcels were released along each tangent point with a time resolution of 1 h. The probability of convective influence along the trajectories was estimated from the high-frequency MSG1 and Himawari geostationary satellites observations of brightness temperature. Both satellite images were used, jointed at the 90° E longitude, to cover the extent of the total AMA region. The trajectory was assumed to encounter a convective event when advected below a deep convective cloud, the top pressure of which was estimated from the brightness temperature, following the same approach as in Tissier and Legras[87].

Trajectories from the ATLAS model[88] were driven by the European Centre for Medium-Range Weather Forecasts ERA Interim reanalysis data (0.75° × 0.75° horizontal resolution, 6 h temporal resolution) and use a log pressure coordinate (kinematic trajectories). The trajectory model includes a detailed stochastic parameterization of convective transport driven by ERA Interim convective mass fluxes and detrainment rates. At every measurement location of GLORIA, 1,000

backward ensemble trajectories are started, which take different paths due to the stochastic nature of the convective transport scheme.

Supplementary Figs. 10 and 11 show backward trajectories starting at the GLORIA measurement locations on 31 Jul 2017 calculated by TRACZILLA and ATLAS, respectively. For the southwest-bound flight leg, exemplary 30 d non-convective backward trajectories are illustrated, starting at locations with NH_3 concentrations enhancement larger than 0.4 ppbv. For the northeast-bound leg, exemplary trajectories starting in the same altitude range (12–14 km) are given for comparison. The trajectories show that the history of the air masses that correspond to enhanced NH_3 concentrations is different from that in which no NH_3 was detected. Further, consistently in both models, the maxima in the convective event density along the trajectories with enhanced NH_3, as indicated by the white contour lines, are located over the Himalayas and the Tibetan plateau, as well as over northwest India and northeast Pakistan. The latter region is clearly correlated with a region of high column amounts as observed by the IASI satellite instruments during the days before the aircraft observations. Thus, we conclude that it is very likely that the high NH_3 concentrations observed by GLORIA were injected into the UT over northwest India and northeast Pakistan by strong convection in a region where, near the ground, high NH_3 concentrations are prevalent.

Data availability

References

49. Möhler, O. et al. Experimental investigation of homogeneous freezing of sulphuric acid particles in the aerosol chamber AIDA. *Atmos. Chem. Phys.* **3**, 211–223 (2003).

50. Fahey, D. W. et al. The AquaVIT-1 intercomparison of atmospheric water vapor measurement techniques. *Atmos. Meas. Tech.* **7**, 3177–3213 (2014).

51. Wagner, R., Benz, S., Möhler, O., Saathoff, H. & Schurath, U. Probing ice clouds by broadband mid-infrared extinction spectroscopy: case studies from ice nucleation experiments in the AIDA aerosol and cloud chamber. *Atmos. Chem. Phys.* **6**, 4775–4800 (2006).

52. Schnaiter, M. et al. Influence of particle size and shape on the backscattering linear depolarisation ratio of small ice crystals—cloud chamber measurements in the context of contrail and cirrus microphysics. *Atmos. Chem. Phys.* **12**, 10465–10484 (2012).

53. Wagner, R. et al. A review of optical measurements at the aerosol and cloud chamber AIDA. *J. Quant. Spectrosc. Radiat. Transf.* **110**, 930–949 (2009).

54. Offermann, D. et al. Cryogenic infrared spectrometers and telescopes for the atmosphere (CRISTA) experiment and middle atmosphere variability. *J. Geophys. Res.* **104**, 16311–16325 (1999).

55. Riese, M. et al. Cryogenic infrared spectrometers and telescopes for the atmosphere (CRISTA) data processing and atmospheric temperature and trace gas retrieval. *J. Geophys. Res.* **104**, 16349–16367 (1999).

56. Grossmann, K. U. et al. The CRISTA-2 mission. *J. Geophys. Res.* **107**, 8173 (2002).

57. Fischer, H. et al. MIPAS: an instrument for atmospheric and climate research. *Atmos. Chem. Phys.* **8**, 2151–2188 (2008).

58. Kleinert, A. et al. Level 0 to 1 processing of the imaging Fourier transform spectrometer GLORIA: generation of radiometrically and spectrally calibrated spectra. *Atmos. Meas. Tech.* **7**, 4167–4184 (2014).

59. Toon, O. B., Tolbert, M. A., Middlebrook, A. M. & Jordan, J. Infrared optical constants of H_2O, ice, amorphous nitric acid solutions, and nitric acid hydrates. *J. Geophys. Res.* **99**, 25631–25654 (1994).

60. Koch, T. G., Holmes, N. S., Roddis, T. B. & Sodeau, J. R. Low-temperature reflection/absorption IR study of thin films of nitric acid hydrates and ammonium nitrate adsorbed on gold foil. *J. Chem. Soc. Faraday Trans.* **92**, 4787 (1996).

61. Biermann, U. M. *Gefrier- und FTIR-Experimente zur Nukleation und Lebensdauer stratosphärischer Wolken.* PhD thesis, Universität Bielefeld (1998).

62. Spang, R. & Remedios, J. J. Observations of a distinctive infra-red spectral feature in the atmospheric spectra of polar stratospheric clouds measured by the CRISTA instrument. *Geophys. Res. Lett.* **30**, 1875 (2003).

63. Höpfner, M. et al. Spectroscopic evidence for NAT, STS, and ice in MIPAS infrared limb emission measurements of polar stratospheric clouds. *Atmos. Chem. Phys.* **6**, 1201–1219 (2006).

64. Woiwode, W. et al. Spectroscopic evidence of large aspherical β-NAT particles involved in denitrification in the December 2011 Arctic stratosphere. *Atmos. Chem. Phys.* **16**, 9505–9532 (2016).

65. Théorêt, A. & Sandorfy, C. Infrared spectra and crystalline phase transitions of ammonium nitrate. *Can. J. Chem.* **42**, 57–62 (1964).

66. Fernandes, J. R., Ganguly, S. & Rao, C. Infrared spectroscopic study of the phase transitions in CsNO₃, RbNO₃ and NH₄NO₃. *Spectrochim. Acta A* **35**, 1013–1020 (1979).
67. Allen, D. T., Palen, E. J., Haimov, M. I., Hering, S. V. & Young, J. R. Fourier transform infrared spectroscopy of aerosol collected in a low pressure impactor (LPI/FTIR): method development and field calibration. *Aerosol Sci. Technol.* **21**, 325–342 (1994).
68. Hopey, J. A., Fuller, K. A., Krishnaswamy, V., Bowdle, D. & Newchurch, M. J. Fourier transform infrared spectroscopy of size-segregated aerosol deposits on foil substrates. *Appl. Opt.* **47**, 2266–2274 (2008).
69. Earle, M. E., Pancescu, R. G., Cosic, B., Zasetsky, A. Y. & Sloan, J. J. Temperature-dependent complex indices of refraction for crystalline (NH₄)₂SO₄. *J. Phys. Chem. A* **110**, 13022–13028 (2006).
70. Rosenoern, T., Schlenker, J. C. & Martin, S. T. Hygroscopic growth of multicomponent aerosol particles influenced by several cycles of relative humidity. *J. Phys. Chem. A* **112**, 2378–2385 (2008).
71. Laskina, O., Young, M. A., Kleiber, P. D. & Grassian, V. H. Infrared extinction spectra of mineral dust aerosol: Single components and complex mixtures. *J. Geophys. Res.* **117**, D18210 (2012).
72. Braban, C. F., Carroll, M. F., Styler, S. A. & Abbatt, J. P. D. Phase transitions of malonic and oxalic acid aerosols. *J. Phys. Chem. A* **107**, 6594–6602 (2003).
73. Miñambres, L., Sánchez, M. N., Castaño, F. & Basterretxea, F. J. Hygroscopic properties of internally mixed particles of ammonium sulfate and succinic acid studied by infrared spectroscopy. *J. Phys. Chem. A* **114**, 6124–6130 (2010).
74. Chasan, D. E. & Norwitz, G. Infrared determination of inorganic nitrates by the pellet technique; infrared determination of two inorganic nitrates in the presence of each other. *Appl. Spectrosc.* **24**, 283–287 (1970).
75. Harris, M. J., Salje, E. K. H. & Guttler, B. K. An infrared spectroscopic study of the internal modes of sodium nitrate: implications for the structural phase transition. *J. Phys. Condens. Matter* **2**, 5517–5527 (1990).
76. Ungermann, J. et al. CRISTA-NF measurements with unprecedented vertical resolution during the RECONCILE aircraft campaign. *Atmos. Meas. Tech.* **5**, 1173–1191 (2012).
77. Sutton, M. A., Erisman, J. W., Dentener, F. & Möller, D. Ammonia in the environment: from ancient times to the present. *Environ. Pollut.* **156**, 583–604 (2008).
78. von Bobrutzki, K. et al. Field inter-comparison of eleven atmospheric ammonia measurement techniques. *Atmos. Meas. Tech.* **3**, 91–112 (2010).
79. von Clarmann, T. et al. Retrieval of temperature, H₂O, O₃, HNO₃, CH₄, N₂O, ClONO₂ and ClO from MIPAS reduced resolution nominal mode limb emission measurements. *Atmos. Meas. Tech.* **2**, 159–175 (2009).
80. Tikhonov, A. On the solution of incorrectly stated problems and method of regularization. *Dokl. Akad. Nauk. SSSR* **151**, 501–504 (1963).
81. Woiwode, W. et al. Validation of first chemistry mode retrieval results from the new limb-imaging FTS GLORIA with correlative MIPAS-STR observations. *Atmos. Meas. Tech.* **8**, 2509–2520 (2015).
82. Johansson, S. et al. Airborne limb-imaging measurements of temperature, HNO₃, O₃, ClONO₂, H₂O and CFC-12 during the Arctic winter 2015/16: characterization, in situ validation and comparison to Aura/MLS. *Atmos. Meas. Tech.* **11**, 4737–4756 (2018).
83. Brands, M. et al. Characterization of a newly developed aircraft-based laser ablation aerosol mass spectrometer (ALABAMA) and first field deployment in urban pollution plumes over Paris during MEGAPOLI 2009. *Aerosol Sci. Technol.* **45**, 46–64 (2011).
84. Murphy, D. M. & Thomson, D. S. Laser ionization mass spectroscopy of single aerosol particles. *Aerosol Sci. Technol.* **22**, 237–249 (1995).
85. Cairo, F. et al. A comparison of light backscattering and particle size distribution measurements in tropical cirrus clouds. *Atmos. Meas. Tech.* **4**, 557–570 (2011).
86. Pisso, I. & Legras, B. Turbulent vertical diffusivity in the sub-tropical stratosphere. *Atmos. Chem. Phys.* **8**, 697–707 (2008).
87. Tissier, A.-S. & Legras, B. Convective sources of trajectories traversing the tropical tropopause layer. *Atmos. Chem. Phys.* **16**, 3383–3398 (2016).
88. Wohltmann, I. & Rex, M. The Lagrangian chemistry and transport model ATLAS: validation of advective transport and mixing. *Geosci. Mod. Dev.* **2**, 153–173 (2009).